RSC Advances

PAPER

View Article Online
View Journal | View Issue



Cite this: *RSC Adv.*, 2019, **9**, 24483

# ZnO nanorod arrays grown on g-$C_3N_4$ micro-sheets for enhanced visible light photocatalytic $H_2$ evolution

Hengfei Qin,[a] Yuanhui Zuo,[a] Jutao Jin,[a] Wenlong Wang,[a] Youlong Xu,[b] Lifeng Cui *[a] and Haifeng Dang *[a]

Received 7th May 2019
Accepted 10th July 2019

DOI: 10.1039/c9ra03426a

rsc.li/rsc-advances

The designed synthesis of noble-metal-free photocatalysts with hierarchical heteroassemblies in a facile, mild and eco-friendly way becomes more and more important, because we can explore the novel properties and applications of novel heterostructures *via* this method. Herein we report a two-step aqueous strategy for novel hierarchical heterostructures of ZnO nanorod (NR) arrays grown on graphitic carbon nitride (g-$C_3N_4$). The novel g-$C_3N_4$/ZnO NR heterostructures that integrate g-$C_3N_4$ and ZnO NR *via* high-quality g-$C_3N_4$–ZnO heterojunctions have beneficial properties such as high specific surface area (SSA), open spatial architecture, good electronic conductivity, and effective charge transfer interfaces, and are promising in many related areas such as water splitting, solar cells, *etc.* As a noble-metal-free and visible-light-responsive photocatalytic material, a typical g-$C_3N_4$/ZnO NR photocatalytic system exhibits enhanced photocatalytic activity toward $H_2$ evolution, almost 3.5 times higher than that of pure g-$C_3N_4$. The superior photocatalytic property can be ascribed to the synergistic effect of the unique g-$C_3N_4$/ZnO NR heterostructures.



## Introduction

With the aggravation of increasing global energy demands and environment issues, the development of clean and renewable energy becomes a promising way to improve the situation.[1] Photocatalysis has attracted increasing attention in the area of photocatalytic water splitting for $H_2$ evolution.[2] Until now, for water splitting photocatalysts, a huge number of semiconductor materials and nanoheterostructures of materials have been searched out.[3–9] Newly, g-$C_3N_4$, a metal-free photocatalyst only consisting of carbon and nitrogen, has been followed closely with worldwide focus due to its various excellent merits, for example, visible light response, high photochemical stability and easily-modified textural/electronic structure.[10] Moreover, ZnO is an important wide-band gap (3.37 eV) and non-toxic semiconductor which has been extensively studied owing to its abundant easy-to-prepare morphologies and high optical, electrical and catalytic properties.[11–20] However, the photocatalytic performance of pristine g-$C_3N_4$ and ZnO are mediocre, mainly because the high recombination ratio of photo-induced electron–hole pairs, the insufficient optical absorption, the small SSA and photocorrosion have limited the practical photocatalytic activity.[21] In order to ameliorate the target materials' photocatalytic properties, many approaches have been presented. Just like the widely reported methods such as doping, morphological-controlled synthesis, coupling and sensitization, have been frequently used for modifying inorganic photocatalysts.[10] Recently, ZnO hybridized with a conjugative π structure material has received special attention. For example, ZnO hybridized with g-$C_3N_4$ has been proved to be an effective method for enhancing photocatalytic activity.[12] Owing to their superior physical/chemical properties, g-$C_3N_4$/ZnO heterostructures have shown higher photocatalytic properties than the pristine. It is generally recognized that the π-conjugated structure promotes separation of charge and transfer efficiency of photoinduced electron–hole pairs at interfaces of semiconductors.[22] As we know, a variety of g-$C_3N_4$/ZnO NR heterostructures with different structures and dimensions have been synthesized including g-$C_3N_4$/ZnO nanoparticles (NPs),[23–25] g-$C_3N_4$/ZnO core–shell structures[26] or g-$C_3N_4$/ZnO core–shell nanoplates (NPLs).[27] However, these heterojunctions mainly consist of isolated phases of the two components. It will certainly create plenty of crystal interfaces with many defects and electron traps, which are detrimental to the transport and output of carriers and the performance of these heterostructure-based devices.[11,28–32] To solve this problem, here we refine the synthetic strategy to a novel advanced hierarchical g-$C_3N_4$/ZnO heterostructure where ZnO NR arrays are growing on the surface of g-$C_3N_4$ which has been realized through a two-step process

[a]*School of Materials Science and Engineering, Dongguan University of Technology, Dongguan 523808, PR China. E-mail: lifeng.cui@gmail.com; cehfdang@163.com*
[b]*Electronic Materials Research Laboratory, Key Laboratory of the Ministry of Education & International Center for Dielectric Research, Xi'an Jiaotong University, Xi'an, 710049, PR China*

involving ZnO seed coating and subsequent heteroepitaxial growth of ZnO NRs (see Scheme 1).[11]

## Results and discussion

Fig. 1 shows the typical heterostrucures of g-$C_3N_4$/ZnO NR heterostructures. From an overview SEM image in Fig. 1a, it can be observed that a delicate herbosa-like heteroassemblies have been fabricated. The g-$C_3N_4$ denoted with the red dotted arrow is the symmetry plane covered by ZnO NR arrays on its both sides. In Fig. 1b, g-$C_3N_4$/ZnO NR heterostructure outlined in yellow is selected for close observation. However, it is difficult to find g-$C_3N_4$ in the heterostructure due to dense covering of ZnO NR arrays on their surfaces. Fig. 1c presents the typical TEM image of g-$C_3N_4$ nanosheet with soft edges. Fig. 1d shows the TEM image of g-$C_3N_4$/ZnO NR heterostructure. It can be seen that ZnO NRs are closely coupled with g-$C_3N_4$.

The XRD pattern of g-$C_3N_4$, ZnO, and g-$C_3N_4$/ZnO heterostructures samples were shown in Fig. 2. It can be seen clearly a strong peak at $2\theta = 27.5°$ corresponding to the characteristic (002) crystal planes of g-$C_3N_4$ and distinct diffraction peak at 31.8°, 34.0°, 36.3°, 47.5°, 56.9°, 62.9° and 68.0° corresponding to the hexagonal-structured wurtzite ZnO (JCPDS, no. 36-1451), which confirms that the heterostructures are composed of g-$C_3N_4$ and ZnO.

The surface chemical composition and chemical state of g-$C_3N_4$/ZnO NRs heterostructure was measured using XPS analysis. As shown in Fig. 3, the survey spectrum shows the distinctive peaks corresponding to carbon (C), nitrogen (N), zinc (Zn), oxygen (O), indicate the formation of g-$C_3N_4$/ZnO heterostructure. The high resolution spectra of the prepared g-$C_3N_4$/ZnO NRs heterostructure was composed of ZnO and g-$C_3N_4$. The spectra of Zn 2p exhibited two major peaks at 1023.63 eV and 1046.47 eV aroused from Zn $2p^3$ and Zn $2p^1$, respectively (Fig. 3a). The position of these peaks illustrates the presence of Zn in the form of ZnO. The broad peak centered at 531.68 eV was related to core level of O in ZnO (Fig. 3b). In case of C 1s, four different peaks were found in deconvoluted spectra (Fig. 3c). The major peak at 284.6 eV stemmed from graphitic carbon nitride phase with low graphitic value. Relatively low

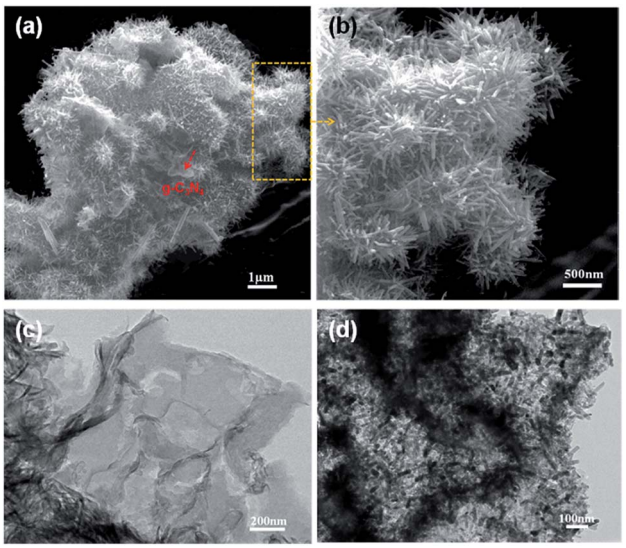


Fig. 1 SEM (a and b), TEM (d) images of g-$C_3N_4$/ZnO NR heterostructure; SEM (c) of pure g-$C_3N_4$.

intense peak at 287.96 eV originated from $sp^2$-hybridized carbon in N-containing aromatic rings C–N=C g-$C_3N_4$ in network. Additional, two peaks at 286.16 eV and 289.26 eV correspond to C=N coordination and OH–C=O bonds, respectively. Finally, high resolution spectra of N 1s displayed three peaks at 398.19 eV, 399.66 eV and 401 eV which are attributed to $sp^2$ nitrogen in triazine ring. The bridging N atoms in N(–C)$_3$ and terminal amino groups (C–N–N) from incomplete condensation during the thermal polymerization process. From these we could say that the heterostructure exhibited ZnO as well as g-$C_3N_4$ phases.

The UV-vis diffuse reflection spectra of dispersed ZnO NRs, bare g-$C_3N_4$ and g-$C_3N_4$/ZnO NRs heterostructures are shown in Fig. 4. Pure g-$C_3N_4$ has photoabsorption from UV light to visible light, with an absorption edge of 471 nm, originating from

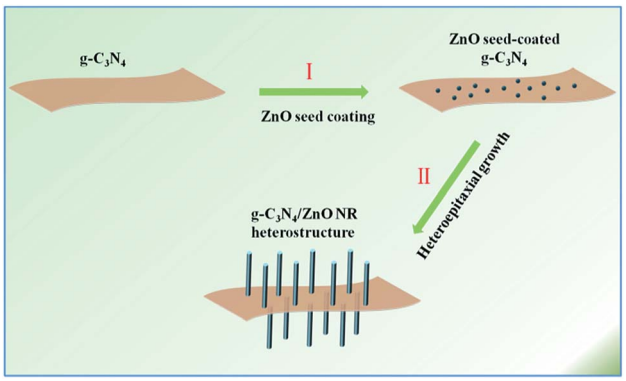


Scheme 1 Schematic illustration of the procedure of hierarchical g-$C_3N_4$/ZnO heterostructure.

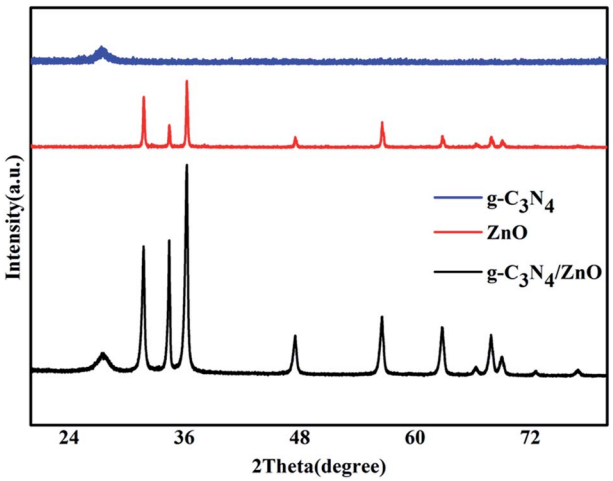


Fig. 2 XRD patterns of the prepared g-$C_3N_4$, ZnO, g-$C_3N_4$/ZnO NR heterostructure.

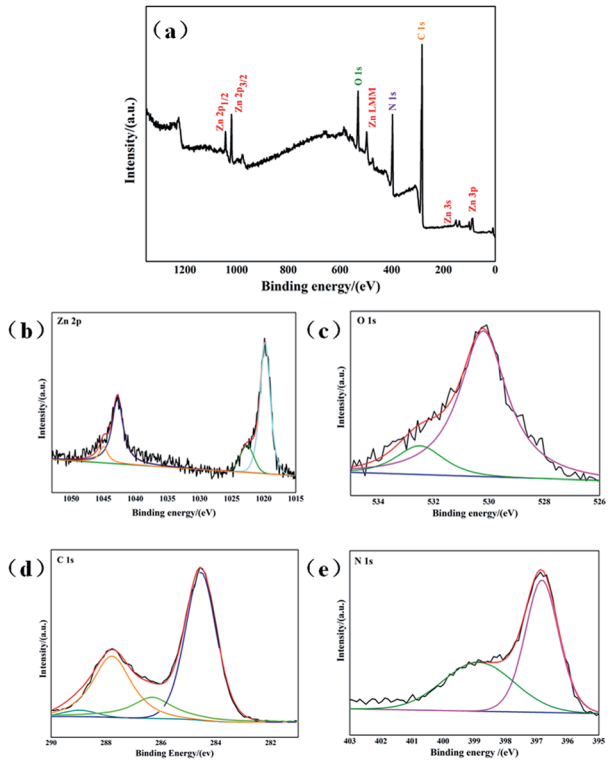


Fig. 3 XPS spectrum of g-$C_3N_4$/ZnO NRs heterostructure (a) survey spectrum, (b) Zn 2p, (c) O 1s, (d) C 1s, (e) N 1s.

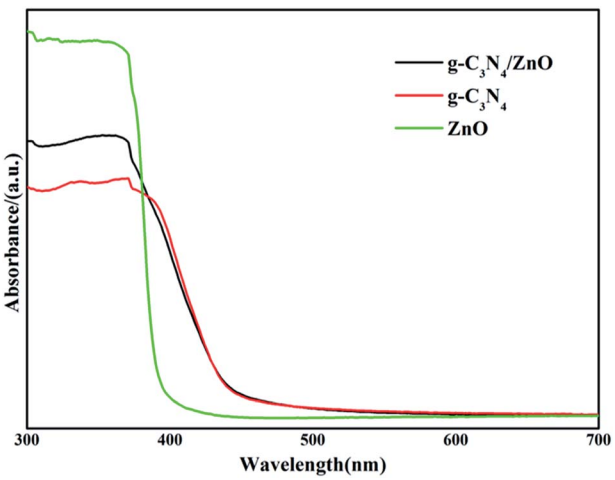


Fig. 4 UV-vis diffuse reflection spectra of the prepared g-$C_3N_4$, ZnO, g-$C_3N_4$/ZnO NR heterostructure.

a band gap of 2.63 eV. In the case of ZnO, only UV light can be absorbed, the band gap is determined to be 3.04 eV. The addition of ZnO shows little effect on the optical property of g-$C_3N_4$. As shown in Fig. 4, the UV-vis spectrum of g-$C_3N_4$/ZnO NRs heterostructure is nearly the same as pure g-$C_3N_4$. The result suggests that g-$C_3N_4$/ZnO NRs heterostructure can absorb visible light.

Photocatalytic $H_2$ production catalyzed by different catalysts was evaluated *via* visible light ($\lambda$ > 400 nm) irradiation in aqueous solution containing 0.2 M $Na_2S$ and 0.5 M $Na_2SO_3$ as sacrificial agents. It can be seen that (Fig. 5), when g-$C_3N_4$ alone was used as photocatalyst, the $H_2$-production rate is not high, which could be ascribed to the rapid recombination of photoinduced carriers generated under visible light. After the combination g-$C_3N_4$ with ZnO, the $H_2$ production performance is significantly enhanced. The $H_2$-production activity of g-$C_3N_4$/ZnO NRs heterostructure under visible light was 3.5 times higher than that of pure g-$C_3N_4$. We also conducted a comparative experiment using a mechanical mixture of g-$C_3N_4$ and ZnO with the optimum composition ratio as the photocatalyst. The result showed that the $H_2$ production rate was much lower than that of g-$C_3N_4$/ZnO sample. We think this remarkable improvement is likely resulted from the unique 2D structure of g-$C_3N_4$ which promotes a faster and more efficient electron transport and export, and significantly enhance the chance for electron acceptors to grasp electron. In brief, firstly, g-$C_3N_4$ connects more ZnO NRs, offering more integrated g-$C_3N_4$–ZnO heterojunctions for better photoinduced hole–electron separation. Secondly, g-$C_3N_4$ can be equivalent to 2D planes consisted of large number of interwoven and serve as spatially-extended electron active centers for electron acceptors (SSA: 31.6 $m^2$ $g^{-1}$). It can be imaged that photogenerated electrons can be transferred directly from the conduction band (CB) of g-$C_3N_4$ to the CB of double-side ZnO NR arrays and the reductive half reactions can be performed, which actually improve the reaction chances and thus prompt the catalysis proceeding.

Recycling performance was carried out to investigate the stability of the composition-optimized product. The $H_2$ generation in different runs is displayed in Fig. 6. No remarkable degradation of $H_2$ generation is observed in the repeated runs for the photocatalytic reaction of 9 h under visible light illumination.

To uncover the separation, transfer of photoinduced eletron–hole pairs at the interfaces of heterostrucures, photoluminescence (PL) spectra was collected to investigate the photogenerated electron–hole pairs separation and electron transfer performance between g-$C_3N_4$ and ZnO.[34,35] The PL spectrum of pure g-$C_3N_4$, mixture of g-$C_3N_4$ and ZnO, and g-

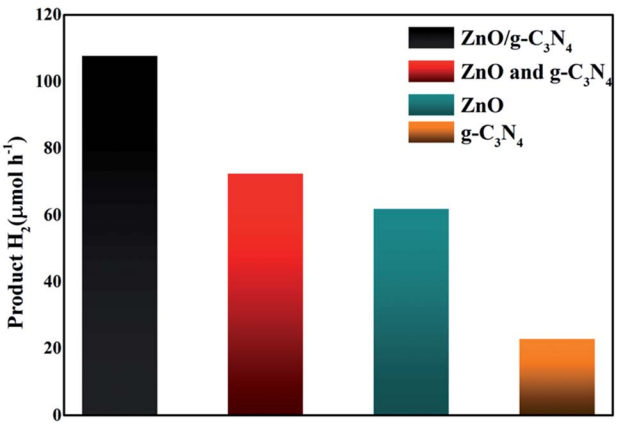


Fig. 5 Photocatalytic $H_2$ evolution on g-$C_3N_4$, ZnO, mixture of g-$C_3N_4$ and ZnO, g-$C_3N_4$/ZnO NR heterostructure.

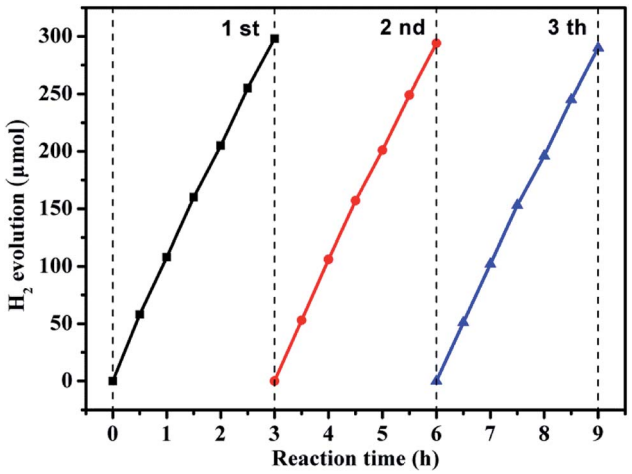


Fig. 6 Reusability experiment for photocatalytic $H_2$ generation by the g-$C_3N_4$/ZnO NR heterostructure under visible light.

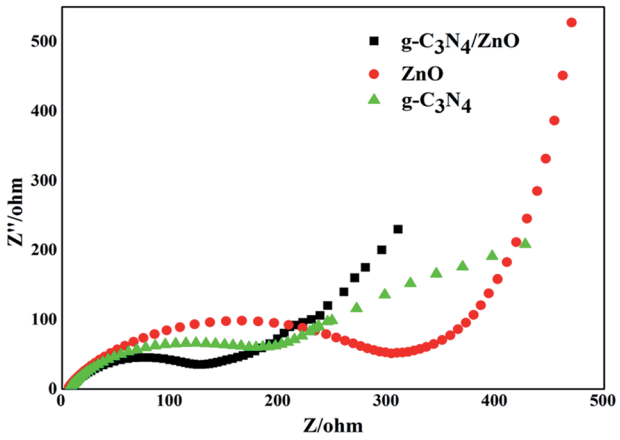


Fig. 8 EIS Nyquist plots of pure ZnO, g-$C_3N_4$ and g-$C_3N_4$/ZnO.

$C_3N_4$/ZnO NRs heterostructure were characterized respectively (Fig. 7). It can be observed that the PL spectrum of pure g-$C_3N_4$ excited at 380 nm showed a strong emission peak at around 445 nm. In the PL spectrum of g-$C_3N_4$/ZnO NRs heterostructure, a weaker emission peak in the same position was detected, suggesting that the addition of ZnO significantly inhibits the recombination of photogenerated electron–hole pairs.[36] For further purposes of comparison, the PL spectrum of the physical mixture of g-$C_3N_4$ and ZnO was also presented. The result suggests that the peak of mixture of g-$C_3N_4$ and ZnO is weaker than that of pure g-$C_3N_4$, but stronger than g-$C_3N_4$/ZnO NRs heterostructure. It confirms that the charge transfer between g-$C_3N_4$ and ZnO would further suppress the recombination of photogenerated electron–hole pairs, which is consistent with the previously described mechanism by Cao *et al.*[33]

Electrochemical impedance spectroscopy tests of pure g-$C_3N_4$, ZnO, and g-$C_3N_4$/ZnO NRs heterostructure were performed to further validate the superior effect of embedded ZnO for improving charge transfer in the samples, and the results are displayed in Fig. 8. The Nyquist plots showed in Fig. 8 were analyzed by a non-linear least squares (NLLS) analysis program. It is well known that the radius of the semicircular arcs on the EIS Nyquist plots reflects the interfacial charge transfer processes occurring on the electrode surface. The larger the arc radius on EIS Nyquist plots, the higher the charge transfer resistance of the sample is. As shown in Fig. 8, the size of the semicircle arc radius of g-$C_3N_4$/ZnO NRs electrode was obviously smaller than that of g-$C_3N_4$ and ZnO electrode. The decreased arc radius on the EIS Nyquist plot of g-$C_3N_4$/ZnO NRs sample implied more efficient separation of photoinduced electron–hole pairs and higher interfacial charge transfer efficiency in the g-$C_3N_4$/ZnO NRs product.

According to the aforementioned results, the proposed mechanism for $H_2$ evolution by the typical g-$C_3N_4$/ZnO NRs sample is demonstrated in Fig. 9. Under visible light irradiation, photo-induced electron–hole pairs are generated on the surface of g-$C_3N_4$, while ZnO itself cannot be excited by visible light. Because the CB position of ZnO (−0.2 eV *vs.* SHE) is lower than that of the conduction bond (CB) of g-$C_3N_4$ (−1.1 eV *vs.* SHE), the photoelectrons generated from g-$C_3N_4$ will inject quickly into the CB of double-side ZnO NR arrays by the well developed interface while photoholes leave in g-$C_3N_4$. During the process, ZnO NR arrays and g-$C_3N_4$ work as both 1D/2D spatial pathways for fast electron/hole transport and spatial

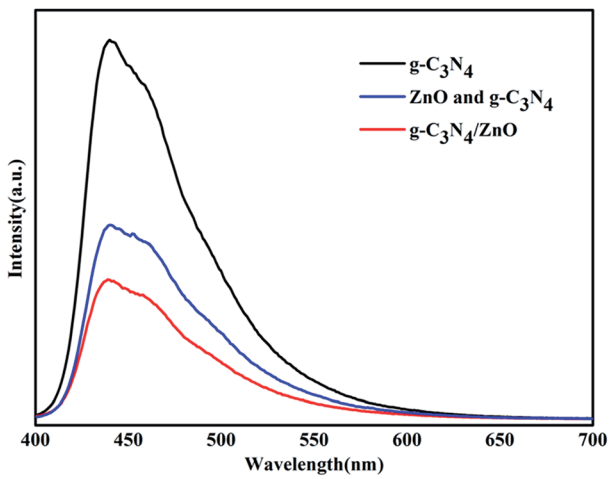


Fig. 7 PL spectra of the prepared g-$C_3N_4$, mixture of g-$C_3N_4$ and ZnO, g-$C_3N_4$/ZnO NR heterostructure.

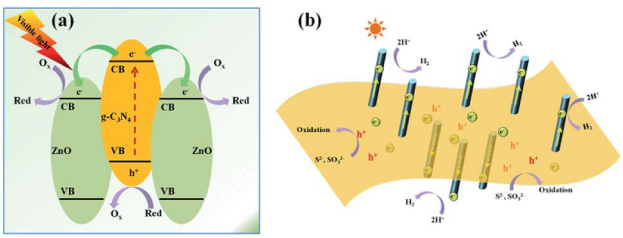


Fig. 9 (a) Schematic illustrations for the photo-induced charge separation over g-$C_3N_4$/ZnO NRs heterostructures. (b) The speculated photocatalytic mechanism over g-$C_3N_4$/ZnO NRs heterostructures.

active sites for efficient catalytic reductive and oxidative reactions. The rapidly proceeding of the oxidative and reductive half reactions leads to the high solar-energy conversion efficiency of photocatalysis. We emphasize here that double-side ZnO NR arrays with opened structure can offer more accessible active sites for $H_2$ formation. As a result, the high photocatalytic $H_2$ production activity was achieved over g-$C_3N_4$/ZnO NRs heterostructures.

# Conclusions

In summary, the novel hierarchical g-$C_3N_4$/ZnO NRs with double-side ZnO NR arrays grown on g-$C_3N_4$ have been fabricated *via* a ZnO-seeded heteroepitaxial growth of ZnO NRs on g-$C_3N_4$. The typical noble-metal-free heterostructure of g-$C_3N_4$/ZnO NRs showed enhanced photocatalytic activity in photocatalytic measurements of $H_2$ evolution compared with the other catalysts under visible light irradiation. The $H_2$ evolution rate of g-$C_3N_4$/ZnO NRs is about 3.5 times higher than that of bare g-$C_3N_4$ catalysts and about 1.8 times relative to bare ZnO catalysts. The remarkable improvement in photocatalytic efficiency is ascribed to the synergistic contribution of the unique structure of the g-$C_3N_4$/ZnO NRs, such as high SSA supplying abundant active sites for effective catalyzing, 1D/2D ZnO NR/g-$C_3N_4$ structures with integrated contact for effective charge separation and high rate 1D/2D electron transport, and special spatial configuration consisting of double side NR arrays and accessible architecture for effective diffusion. With these structural advantages, the novel g-$C_3N_4$/ZnO heterostructures when made some suitable modifications also are promising in many related areas such as energy conversion and storage, electro-chemistry and so on.

# Experimental

### Materials

The urea (99%) used in the experiment was supplied by Sigma-Aldrich. All of the other chemical reagents were of analytical grade without further purification, and all the water used in the experiment was deionized water.

### Preparation of g-$C_3N_4$

About 15 g of urea was put in a quartz crucible with a cover and was heated at 550 °C for 2 h in air. In addition, the heating rate was 2 °C min.

### Preparation of g-$C_3N_4$/ZnO heterostructure

For a typical synthesis, firstly, the g-$C_3N_4$ powder were dispersed in 1 g $L^{-1}$ poly-(vinylpyrrolidone) (PVP) aqueous solution for 2 h, followed by washing with ethanol several times to remove excessive adsorbed PVP molecules. Next, the PVP-treated g-$C_3N_4$ were soaked in the pre-prepared ZnO seed solution.[9] Four hours later, the g-$C_3N_4$ with coated ZnO seeds were centrifugalized and washed with ethanol twice. Then, the obtained ZnO seed-coated g-$C_3N_4$ sample were scattered around in a 40 mL aqueous solution composed of equimolar zinc acetate ($Zn(CH_3COO)_2$, 0.02 M) and hexamethylenetetramine (HMT, 0.02 M). After incubation at 85 °C for 6 h, the product was separated with the centrifuge method, washed by deionized water several times, dried in stove and reserved for further use.

### Characterization

The morphology of g-$C_3N_4$/ZnO NR heterostructures was characterized using a field emission scanning electron microscope (FESEM, JSM-7000F, 5 kV) and high-resolution transmission electron microscopy (HR-TEM, JEM 2011, acceleration voltage 200 kV). The crystal structure was determined by X-ray diffraction (XRD) using a D8 Advance X-ray diffractometer with Cu K$\alpha$ radiation with a 1.5418 Å wavelength (Bruker AXS, German). The accelerating voltage of 40 kV and a 40 mA applied current beam were used. X-ray photoelectron spectroscopy (XPS) was characterized on a Thermo Fisher Scientific Escalab 250 spectrometer with monochromatized Al K$\alpha$ radiation. UV-vis diffuse reflectance spectra of the samples were performed on a Cary-50 UV-vis spectrophotometer. Photoluminescence (PL) spectra were recorded at room temperature with a fluorescence spectrophotometer (F-7000, Hitachi, Japan). The excitation wavelength was 380 nm. The Brunauer–Emmett–Teller (BET) surface area of the sample was evaluated by $N_2$ adsorption–desorption measurements at 77 K in an automated surface area and porosity analyzer (ASAP2020, Micromeritics, USA).

### Evaluation of photocatalytic $H_2$ evolution

The photocatalytic reactions were carried out in a quartz reaction vessel connected to a closed gas circulation and evacuation system. The diameter of the quartz container was 7.5 cm, and the height was 12 cm. A 300 W Xe lamp (HSX-F/UV 300, Bjnbet Co., Ltd., China) equipped with a UV cut-off filter ($\lambda$ > 400 nm) was used as the visible light source and the integrated light intensity on the reaction reactor was about 60 mW $cm^{-2}$. The temperature of the reaction system was maintained at *ca.* 293 K through programmed temperature control device. Before each experiment, the closed system was degassed with $N_2$ for 0.5 h to drive away the $O_2$. For each experiment, 0.1 g catalyst was suspended into 250 mL aqueous solution with 0.2 M $Na_2S$ and 0.5 M $Na_2SO_3$ as sacrificial reagent. The gas product was examined with an on-line gas chromatography with a thermal conductivity detector (GC2600, $N_2$ carrier, 5A molecular sieve column).

# Conflicts of interest

There are no conflicts to declare.

# Acknowledgements

This research was supported by Startup Research Fund of Dongguan University of Technology (KCYKYQD2017015) and Training Program of Innovation and Entrepreneurship for Undergraduates of Dongguan University of Technology (201911819133).

## Notes and references

1 Z. A. Huang, Q. Sun, K. L. Lv, Z. H. Zhang, M. Li and B. Li, *Appl. Catal., B*, 2015, **164**, 420.
2 X. Q. Fan, L. X. Zhang, R. L. Cheng, M. Wang, M. L. Li, Y. J. Zhou and J. L. Shi, *ACS Catal.*, 2015, **5**, 5008.
3 S. E. Habas, P. D. Yang and T. J. Mokari, *J. Am. Chem. Soc.*, 2008, **130**, 3294.
4 C. Pacholski, A. Kornowski and H. Weller, *Angew. Chem., Int. Ed.*, 2004, **43**, 4774.
5 F. R. Fan, Y. Ding, D. Y. Liu, Z. Q. Tian and Z. L. Wang, *J. Am. Chem. Soc.*, 2009, **131**, 12036.
6 K. Sun, Y. Jing, N. Park, C. H. Li, Y. S. Bando and D. L. Wang, *J. Am. Chem. Soc.*, 2010, **132**, 15465.
7 J. S. Lee, E. V. Shevchenko and D. V. Talapin, *J. Am. Chem. Soc.*, 2008, **130**, 9673.
8 L. Wu, B. G. Quan, Y. L. Liu, R. Song and Z. Y. Tang, *ACS Nano*, 2011, **5**, 2224.
9 J. Yang and J. Y. Ying, *Angew. Chem., Int. Ed.*, 2011, **50**, 4637.
10 Y. M. He, Y. Wang, L. H. Zhang, B. T. Teng and M. H. Fan, *Appl. Catal., B*, 2015, **168**, 1.
11 Y. H. Zuo, Y. Qin, C. Jin, Y. Li, S. D. Shi, Q. S. Wu and J. H. Yang, *Nanoscale*, 2013, **5**, 4388.
12 A. I. Hochbaum and P. D. Yang, *Chem. Rev.*, 2010, **110**, 527.
13 Z. W. Pan, Z. R. Dai and Z. L. Wang, *Science*, 2001, **291**, 1947.
14 Z. L. Wang and J. H. Song, *Science*, 2006, **312**, 242.
15 J. Yin, Y. S. Zang, C. Yue, Z. M. Wu, S. T. Wu, J. Li and Z. H. Wu, *J. Mater. Chem.*, 2012, **22**, 7902.
16 M. H. Huang, S. Mao, H. Feick, H. Q. Yan, Y. Y. Wu, H. Kind, E. Weber, R. Russo and P. D. Yang, *Science*, 2001, **292**, 1897.
17 S. H. Ko, D. Lee, H. W. Kang, K. H. Nam, J. Y. Yeo, S. J. Hong, C. P. Grigoropoulos and H. J. Sung, *Nano Lett.*, 2011, **11**, 666.
18 M. H. Hsu, C. J. Chang and H. T. Weng, *ACS Sustainable Chem. Eng.*, 2016, **4**, 1381.
19 M. H. Hsu and C. J. Chang, *Int. J. Hydrogen Energy*, 2014, **39**, 16524.
20 M. H. Hsu and C. J. Chang, *J. Hazard. Mater.*, 2014, **278**, 444.
21 D. C. Chen, K. W. Wang, D. G. Xiang, R. L. Zong, W. Q. Yao and Y. F. Zhu, *Appl. Catal., B*, 2014, **147**, 554.
22 Y. J. Wang, R. Shi, J. Lin and Y. F. Zhu, *Energy Environ. Sci.*, 2011, **4**, 2922.
23 C. Liu, C. M. Li, X. D. Fu, F. Z. Raziq, Y. Qu and L. Q. Jing, *RSC Adv.*, 2015, **5**, 37275.
24 W. Liu, M. L. Wang, C. X. Xu and S. F. Chen, *Chem. Eng. J.*, 2012, **5**, 386.
25 W. Liu, M. L. Wang, C. X. Xu, S. F. Chen and X. L. Fu, *J. Mol. Catal. A: Chem.*, 2013, **368**, 9.
26 J. Wang, Y. Xia, H. Y. Zhao, G. F. Wang, L. Xiang and J. L. Xu, *Appl. Catal., B*, 2006, **63**, 305.
27 S. Kumar, A. Baruah, S. Tonda, B. Kumar, V. Shanker and B. Sreedhar, *Nanoscale*, 2014, **6**, 4830.
28 J. X. Sun, Y. P. Yuan, L. G. Qiu, X. Jiang, A. J. Xie, Y. H. Shen and J. F. Zhu, *Dalton Trans.*, 2012, **41**, 6756.
29 R. Hao, G. H. Wang, H. Tang, L. L. Sun, C. Xu and D. Y. Han, *Appl. Catal., B*, 2016, **187**, 47.
30 J. W. Zhou, M. Zhang and Y. F. Zhu, *Phys. Chem. Chem. Phys.*, 2015, **17**, 3647.
31 D. M. Chen, K. W. Wang, T. Z. Ren, H. Ding and Y. F. Zhu, *Dalton Trans.*, 2014, **43**, 13105.
32 L. Zu, Y. Qin and J. Yang, *J. Mater. Chem. A*, 2015, **3**, 10209.
33 S. W. Cao, X. F. Liu, Y. P. Yuan, Z. Y. Zhang, Y. S. Liao, J. Fang, S. C. Joachim Loo, T. C. Sun and C. Xue, *Appl. Catal., B*, 2014, **147**, 940.
34 W. K. Jo, J. Y. Lee and N. C. S. Selvam, *Chem. Eng. J.*, 2016, **289**, 306.
35 H. Dang, G. Tan, W. Yang, F. Su, H. Fan, X. Dong and L. Ye, *J. Taiwan Inst. Chem. Eng.*, 2017, **78**, 185.
36 J. Wang, Z. Yang, X. Gao, W. Yao, W. Wei, X. Chen, R. Zong and Y. Zhu, *Appl. Catal., B*, 2017, **217**, 169.